

JGR Space Physics

RESEARCH ARTICLE

10.1029/2021JA029795

Key Points:

- The role of plasma convection in the formation of the polar holes is investigated
- Polar holes has larger latitudinal extent than previously thought
- Plasma does not have to be trapped in the closed convection loops is full darkness to become depleted

Correspondence to:

V. V. Forsythe, victoriyaforsythe@gmail.com

Citation

Forsythe, V. V., Kunduri, B., & Zou, S. (2021). Multi-instrument investigation of the polar holes. *Journal of Geophysical Research: Space Physics*, 126, e2021JA029795. https://doi.org/10.1029/2021JA029795

Received 14 JUL 2021 Accepted 8 NOV 2021

Multi-Instrument Investigation of the Polar Holes

Victoriya V. Forsythe¹, Bharat Kunduri², and Shasha Zou³

¹ASTRA LLC., Louisville, CO, USA, ²Virginia Polytechnic Institute and State University, Blacksburg, VA, USA, ³Department of Climate and Space Sciences and Engineering, University of Michigan, Ann Arbor, MI, USA

Abstract During the solar minimum the F-region plasma density can become extremely low, and in some exceptional cases the F-layer can completely disappear. These F-region density depletions are particularly deep during geomagnetically quiet nights, when slow plasma convection creates polar holes, extending 100-1000 km in size, where the electron density is several orders of magnitude lower than the background values. Polar holes are believed to be formed during the periods of the very slow anti-sunward convection, when the plasma is trapped just poleward of the auroral oval in the absence of any ionization sources. At the same time, fast convection with rapid vertical plasma transport has also been associated with the polar hole formation. Combining the electron density measurements from the Resolute Bay Incoherent Scatter Radar (RISR) and Poker Flat ISR (PFISR), the state of art variational data assimilation tool Ionospheric Data Assimilation Four-Dimensional (IDA4D), and the convection data from the Super Dual Auroral Radar Network (SuperDARN) array, the polar hole formation and evolution are experimentally investigated. The F-region plasma is traced back in time prior to the polar hole formation to analyze the favorable conditions for the formation of the polar holes. The role of plasma convection in the formation of the polar holes is experimentally investigated. The results show that the polar holes can be formed in the twilight condition and without being trapped in the closed convection loops. The formation of the polar holes were equally possible during slow and strong convection flows, predominantly with a standard two-cell convection configuration.

1. Introduction

In order to fully understand the behavior of the ionosphere as a system, it is essential to understand its extremes. Large areas of the polar region with exceptionally low plasma densities known as polar holes represent an extreme of the ionospheric plasma environment. The behavior near the other extreme of high density has attracted much attention over the years, including numerous studies of polar patches (review by Carlson, 2012) and storm enhanced density (review by Foster et al., 2021). In contrast, the low-density extreme remains much less explored. In particular, formation mechanisms of the polar holes have not been established experimentally.

From the discovery (Brinton et al., 1978) to the modeling simulations (Sojka et al., 1981a, 1981b) of the polar holes, slow plasma convection has been thought to be the key factor responsible for their formation. Modeling studies concluded that the formation of the polar hole during geomagnetically quiet time may occur during continuous recombination over a long interval when the plasma is moving within slow convection in darkness and in the absence of an ionization source (Sojka et al., 1981a, 1981b). The expected location of the polar hole during slow convection is in the 21–06 magnetic local time (MLT), 70–80° magnetic latitude sector (Brinton et al., 1978), where the convection is expected to be anti-sunward. In this region, a component of the anti-sunward convection speed is expected to be approximately equal and opposite to the co-rotation speed, and the plasma therefore moves extremely slow in the solar inertial reference frame (Sojka et al., 1981a). However, this straightforward mechanism has not been experimentally verified.

The study by Sojka et al. (1981c) proposed a new mechanism where the slow convection is not necessarily required. For the magnetically active conditions, the polar hole was proposed to be formed during strong convection and large downward plasma transport driven by strong electric field (Sojka et al., 1981c). The location of the expected polar hole that would be formed under the magnetically active conditions is colocated with the regions of large downward plasma drifts inside of the 80° magnetic sector. An experimental study by Makarevich et al. (2015) concluded that neither slow nor fast convection accompanied the density depressions in the winter polar cap. This suggested that the role of plasma convection needs to undergo the additional investigation.

© 2021. American Geophysical Union. All Rights Reserved.

FORSYTHE ET AL. 1 of 19



Early polar hole studies monitored the density in the ionosphere along the satellite passes (Brinton et al., 1978; Crowley et al., 1993; Hoegy & Grebowsky, 1991) and using ionosondes (Benson & Grebowsky, 2001; Crowley et al., 1993). Nowadays the existing instruments allow more comprehensive studies of the polar holes. Three Incoherent Scatter Radars (ISRs) in the Northern Hemisphere are employed in this study to detect polar holes. The Resolute Bay Incoherent Scatter Radar (RISR) facility in the northern polar cap consists of two faces, the northern face (RISR-N) face and the Canadian face (RISR-C), and, as a combined facility, it overlooks the geomagnetic polar cap region and the region where the statistical polar hole occurs (Brinton et al., 1978; Sojka et al., 1981a). Additionally, the PFISR system provides information about the electron density in the auroral or subauroral zone. This enables direct investigations of the density depletion region and its vicinity.

Previous studies that investigated the role of convection in the polar hole formation used statistical convection patterns (Sojka & Schunk, 1987) because the concurrent measurements were not available at the time. Nowadays, Super Dual Auroral Radar Network (SuperDARN) continuously provides information about the global plasma convection in the high-latitude and polar ionosphere. SuperDARN is a powerful instrument for plasma convection studies and has been proven to be successful for tracking the polar patches (Oksavik et al., 2010; Ren et al., 2020; Thomas et al., 2015). However, it has not yet been used for studies of the polar holes. In this paper SuperDARN is employed to see what configurations of the convection lead to the formation of the polar holes, analyzing the history of the convection prior to the polar hole formation.

Ionospheric Data Assimilation Four-Dimensional (IDA4D) technique (Bust et al., 2000, 2001, 2004) is used in this study to determine the horizontal extent of the polar holes, to investigate their evolution and their global position in relation to other density structures such as ionospheric troughs. IDA4D is an ionospheric spatial analysis algorithm that uses multiple data sources to obtain a global specification of electron density (Bust et al., 2004). IDA4D has been successfully used to study the evolution of polar cap patches in the northern polar cap (Bust & Crowley, 2007) and large-scale plasma variations in the southern polar cap (Kinrade et al., 2012). In this study, the IDA4D provides the synoptic information about the electron density on large spatial scale, once the polar hole events are identified with ISR data.

This study aims to experimentally establish the role of convection in the formation and evolution of the polar holes by using direct radar observations of convection and density together with data assimilation results.

2. Experimental Setup

2.1. Incoherent Scatter Radars

Figure 1 shows the experimental setup used in this investigation. The data from three incoherent scatter radars (ISR) were analyzed to find the density depletion events. The yellow areas in Figure 1 show the footprints of the RISR system with its northern (RISR-N) and Canadian (RISR-C) faces, and Poker Flat ISR (PFISR). RISR and PFISR consist of an electronically steerable phased array that allows to take measurements in many directions within the viewing area with a very high time cadence (Bahcivan et al., 2010). The radars measure the electron density, ion and electron temperatures, and ion drift velocity obtained from the power spectra using standard ISR technique (Evans, 1969; Nicolls et al., 2007; Rishbeth & Williams, 1985). More details about calibration techniques can also be found in studies by Bahcivan et al. (2010) and Themens et al. (2014). Only the vertical electron density profiles obtained in Long Pulse (LP) Mode were selected for the search of the events. For RISR-N and RISR-C the beams with elevation angle of 75° were chosen over the beams with 90° elevation to avoid a grating lobe issue.

2.2. High Frequency Radars

The high-latitude convection measurements from the Super Dual Auroral Radar Network (SuperDARN) (Chisham et al., 2007; Greenwald et al., 1995) were employed in this study to track the plasma prior to the polar hole events. The gray fan areas in Figure 1 show the footprints of the SuperDARN radars that measure the line-of-sight F region velocity of plasma convection. The line-of-sight data are then combined in a standard SuperDARN algorithm to produce electrostatic potential and convection patterns using the map potential technique (Ruohoniemi & Baker, 1998).

FORSYTHE ET AL. 2 of 19

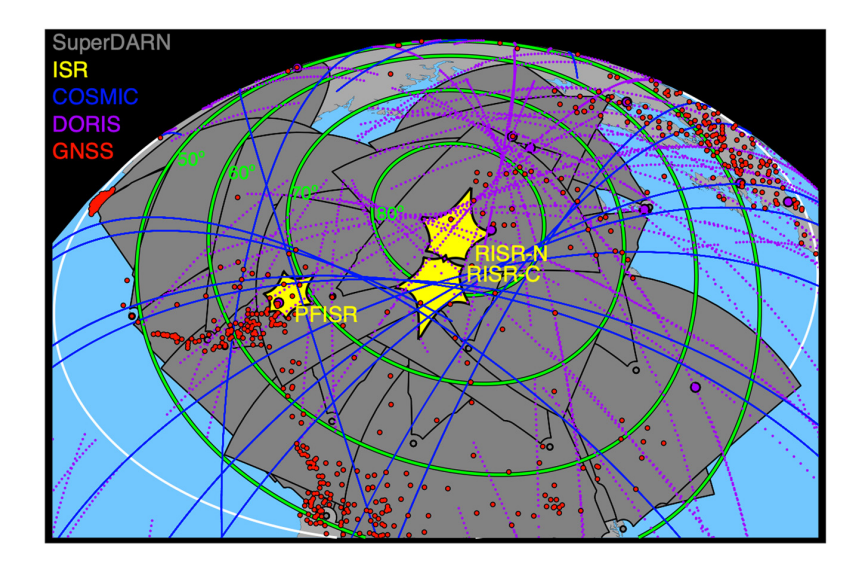


Figure 1. Experimental setup of the polar hole investigation. The fields of view of three Incoherent Scatter Radars are shown with yellow. The fan footprints of SuperDARN radars are shown with gray. Red dots show the locations of GNSS ground-based receivers. The paths of COSMIC satellites are during September 20, 2020, 00–04 UT are shown with blue curves. The paths of DORIS SPOT-4 and SPOT-5 satellites during the day of September 20, 2020 are shown with purple dots. The ground-based DORIS transmitters are shown with purple circles. Magnetic latitudes of 80°, 70°, 60°, and 50°N based on the altitude-adjusted corrected geomagnetic (AACGM) coordinate system with 2010 coefficients (Shepherd, 2014) are shown with green. White curve shows the lowest latitudinal boundary of IDA4D grid.

2.3. Ionospheric Data Assimilation

The information about the position and the horizontal extent of the polar holes were obtained using the runs of the Ionospheric Data Assimilation Four-Dimensional (IDA4D). IDA4D is an objective analysis maximum-likelihood algorithm that estimates the global, 3-D time-varying distribution of electron density between 90 and 600 km altitudes (Bust & Crowley, 2007; Bust & Datta-Barua, 2014; Bust & Mitchell, 2008; Bust et al., 2001, 2004; Datta-Barua et al., 2011). The IDA4D algorithm is closely based on the Naval Research Laboratory's meteorological 3-D variation (3DVAR) data assimilation scheme (Daley & Barker, 2000). The high-latitude grid was used for the assimilation, with the lowest latitude boundary of 41°N shown with white curve in Figure 1. The data that were ingested by IDA4D consisted of slant total electron content (sTEC) measurements obtained using three different types of observations. First type represents the sTEC measured between GNSS satellites and ground-based GNSS receivers shown with red dots in Figure 1. Second type of sTEC is measured between GNSS satellites and receivers on board of Low Earth Orbit (LEO) Constellation Observing System for Meteorology, Ionosphere, and Climate (COSMIC) satellites, which paths are shown with blue curves in Figure 1 for the day of September 20, 2009, 00-04 UT. Third type of sTEC is observed between ground-based transmitters, shown with purple circles, and receivers on board of Doppler Orbitography and Radiopositioning Integrated by Satellite (DORIS) SPOT-4 and SPOT-5, which paths are shown with purple dots for the day of September 20, 2009. SPOT-4 and SPOT-5 stopped their operation after June 2013 and December 2015, respectively, therefore not all the events considered in this study benefited from their data.

3. Observations

The ISR data were examined to identify events with unusually low electron density. For the selected events the electron density at 300 km altitude must be on average one order of magnitude lower than the IRI prediction during a continuous period of time (at least 2 hr). The altitude of 300 km was considered in this study for the event selection because the same altitude was considered in the initial studies of the polar holes (Brinton et al., 1978; Hoegy & Grebowsky, 1991).

The density criterion in this study is stricter in comparison to other studies. For example, Makarevich et al. (2015) investigated events where 1% of RISR-N measurements at 300 km had $N_{\rm e} < 4 \times 10^{10} \ {\rm m}^{-3}$ and at least 10% of

FORSYTHE ET AL. 3 of 19

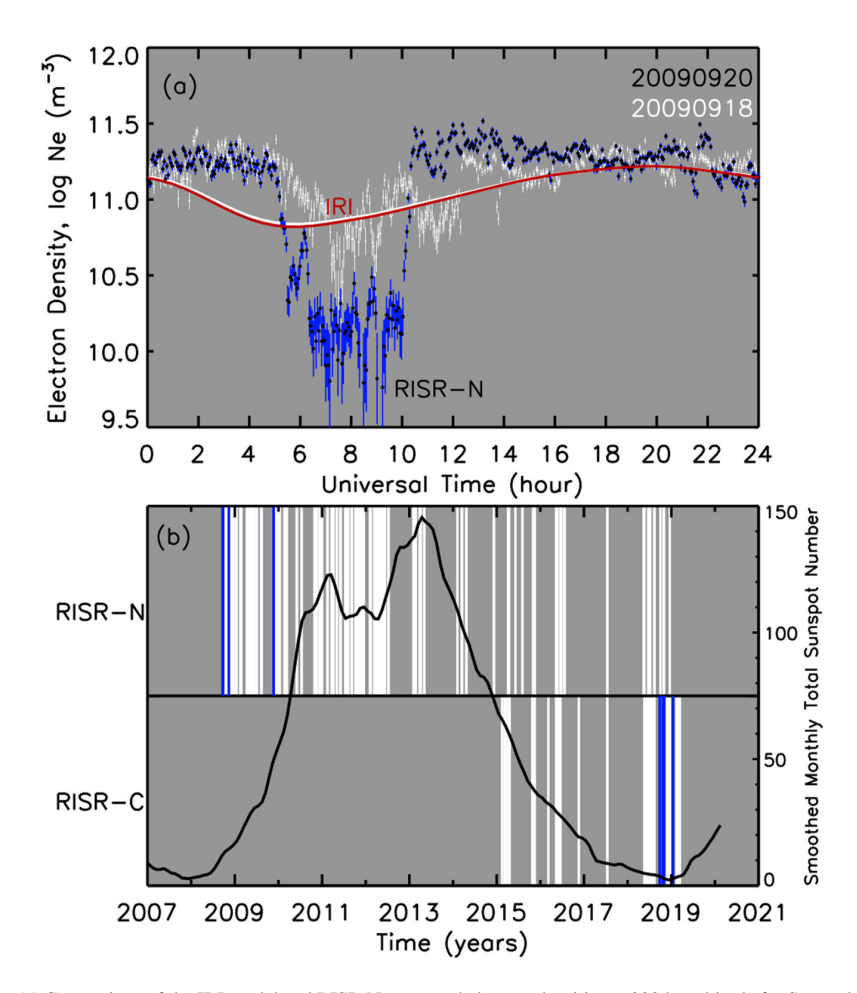


Figure 2. (a) Comparison of the IRI model and RISR-N measured electron densities at 300 km altitude for September 20, 2009. IRI prediction is shown with red curve, whereas RISR-N measurements are shown with black dots. Uncertainties in the measured density are shown by the vertical blue lines. Additionally, RISR-N measurements with uncertainties for September 18, 2009 and the IRI prediction for that day are shown with white. (b) White stripes show the days when RISR-N or RISR-C data were available. Blue lines indicate the days of the selected events. Additionally, black curve shows the 13-month smoothed monthly total sunspot number for the Solar Cycle 24.

measurements with $N_{\rm e}$ < 10^{11} m⁻³. Additionally, the study of Crowley et al. (1993) indicated the polar hole in the Qanaq digisonde $N_{\rm m}F_2$ observations as a drop from 4×10^{11} m⁻³ to 10^{11} m⁻³, which is not as deep as what was considered here.

More events could have been found for the current investigation in case the selection criteria are eased. For instance, six other events satisfied the minimum density requirement but were shorter than 2 hr in duration, whereas 7 additional events satisfied the duration requirement, but had large uncertainties of the low-density measurements, making it challenging to state that the density is one order of magnitude lower than the IRI density. This study does not claim that these additional events do not belong to the category of the polar holes. Instead, the strict selection criteria guarantee that the 9 considered events are most likely the polar holes.

Figure 2a shows a comparison of the IRI model (shown with red curve) and RISR-N measured electron densities (shown with black dots) at 300 km altitude for September 20, 2009. Uncertainties in the measured density are shown by the vertical blue lines. An abrupt decrease of density was observed by RISR-N at 5–11 UT, which corresponds to 22–4 MLT. Even with the uncertainties of the measurements, this difference between the observations and the IRI trend is significant. Additionally, white color in Figure 2a shows RISR-N measurements and IRI prediction for September 18, 2009, which is a day with similar solar and geomagnetic conditions, but without

FORSYTHE ET AL. 4 of 19

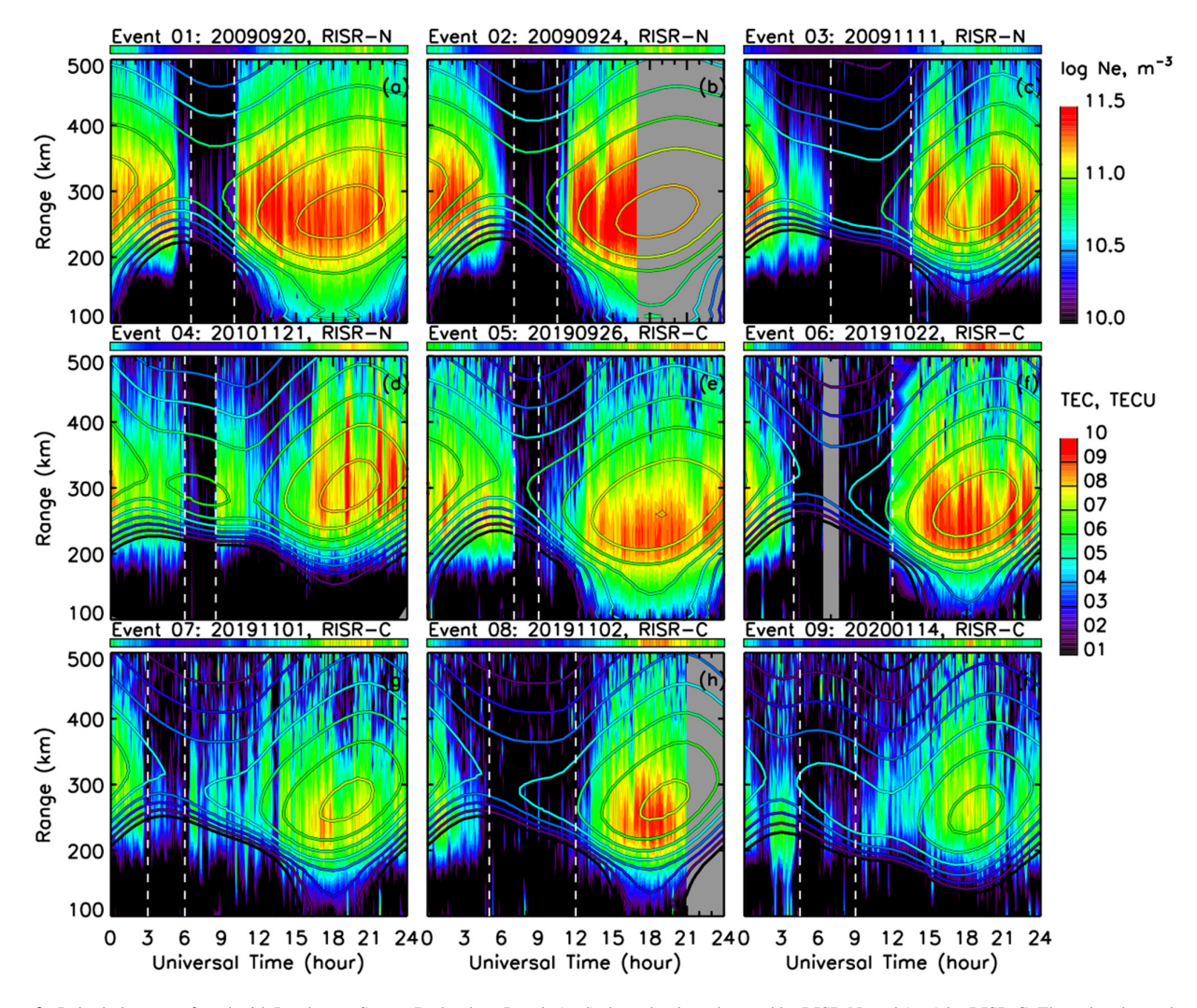


Figure 3. Polar hole events found with Incoherent Scatter Radar data. Panels (a–d) show the data observed by RISR-N, and (e–g) by RISR-C. The color shows the electron density, with the color bar shown on the right of the Figure. The colored contours show the electron density expected by the IRI-2016 model. The colored line on top of each panel shows the TEC above the radar, obtained by the IDA4D, with the color bar on the right of the figure. Vertical dashed lines show the approximate times for the beginning and end of the polar hole events.

a polar hole presence. During a regular day, the density measurements do not show any significant deviation from the IRI trend, besides the time when the IRI underestimates density from 0–5 UT, which is consistent with Themens et al. (2014). However, the polar hole event showed significant deviation even from the underestimated IRI trend.

White stripes in Figure 2b show the days when the RISR-N and RISR-C data were available. Blue stripes show the days that satisfy the criteria for the polar hole selection. The black curve in Figure 2b also shows the smoothed monthly total sunspot number for the Solar Cycle 24. As expected, the selected events occurred during solar minimum, since polar holes are the solar minimum phenomena (for example, Crowley et al., 1993; Hoegy & Grebowsky, 1991).

Figure 3 shows all nine events. Four events were observed by RISR-N (Figures 3a–3d), and five events by RISR-C (Figures 3e–3i). The background color in Figure 3 shows the electron density observed by ISR, whereas the contours represent the electron density expected by the International Reference Ionosphere (IRI-2016) (Bilitza et al., 2017) model. The white vertical dashed lines show the approximate beginning and the end of the depletion

FORSYTHE ET AL. 5 of 19



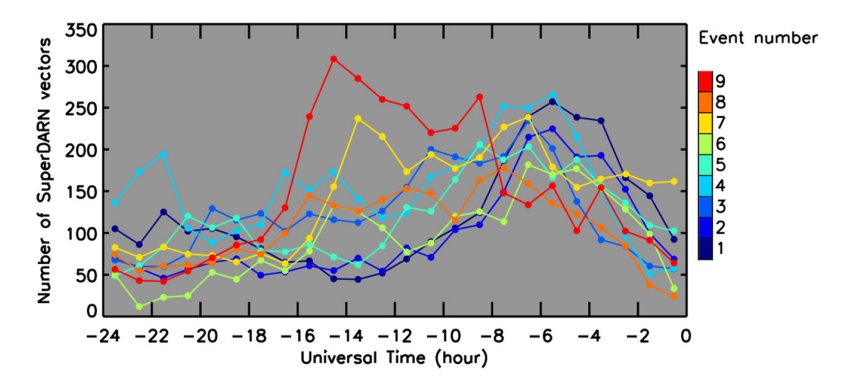


Figure 4. 1-hr averaged number of SuperDARN vectors prior to the polar hole observation for 9 events.

events. All of the events shown in Figure 3 have a sudden arrival of the low density into the field of view of the radar. All nine events occurred during low geomagnetic activity, with the daily $Kp \le 1$.

IDA4D results were obtained for the days of the events and one day prior to the days of the events. The color stripes on top of the panels in Figure 3 show the vertical total electron content (vTEC) estimated by IDA4D at the radar's location. The depletion in vTEC estimated by IDA4D agrees in most cases with the occurrence of the density depletion observed by ISRs.

The SuperDARN convection maps were also obtained for the days of the events to trace the motion of plasma back in time prior to the formation of the depletion. In order to check the reliability of these maps, the amount of back-scatter was analyzed first. Figure 4 shows the 1-hr averaged number of SuperDARN vectors resolved from back-scatter that were used to produce two-dimensional plasma velocity maps. The color of the lines corresponds to the event number, with the color bar shown on the right of the Figure. In general, for a SuperDARN radar to detect ionospheric echoes, the irregularities must be present and the radio signal needs to become orthogonal to the

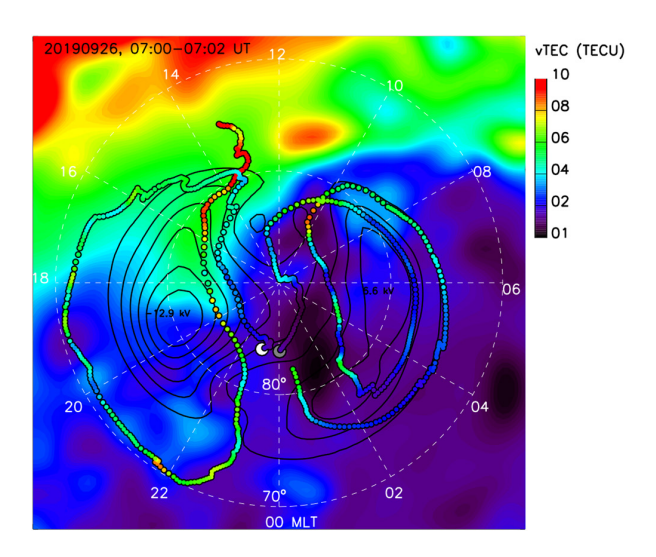


Figure 5. The background color shows the vTEC output of IDA4D for the event number 5 (20,190,926) at 7:00-7:02 UT, the time when RISR-C detected very low density. The black contours show the configuration of the cross polar cap potential derived from the SuperDARN data for that time frame, with the lowest and the highest potential values of -12.9 and 5.6 kV. White and gray circles show the locations of RISR-C at 7:00 UT and 8:00 UT, respectively. The colored circles connected to these locations show the 12-hr back in time trace of plasma, color-coded in vTEC, with the color bar shown on the right of the figure.

Earth's magnetic field. It is not an easy task to explain the diurnal variation of the ionospheric echo occurrence for a single SuperDARN radar (for example Koustov et al., 2019), moreover, for several radars at the same time. Nevertheless, Figure 4 shows that the number of observations was at maximum for most of the events (except event number 9) withing 12-hr period prior to the polar hole detection. Even though, there is no minimum cut-off number of vectors to consider the individual map reliable, it is reassuring to know that the occurrence of back-scatter was as high as it can be to investigate the history of the plasma motion.

Figure 5 shows the IDA4D vTEC output for the event number 5, shown in Figure 3e, that occurred on September 26, 2019. The time frame of 07:00-07:02 UT corresponds to the beginning of the event, indicated by the first dashed line in Figure 3e. A region with a very low (less than 2 TECU) TEC is present inside the polar cap. It is also evident that low vTEC regions were present at lower latitudes (less than 70°N), where the high-latitude troughs are normally observed. The black contours in Figure 5 show the SuperDARN equipotential for the same time frame, with the lowest and the highest potential values of -12.9 and 5.6 kV, respectively. The plasma convection for this time frame has a standard two-cell configuration. The white circle shows the location of RISR-C at 7:00 UT. Using the SuperDARN plasma velocity maps, the test particle was placed at the location of the radar and traced back in time, saving the information about the plasma velocity magnitude and direction, vTEC, and solar zenith angle (SZA) at the locations of the trace. The colored circles in Figure 5 that are connected to the location of RISR-C show the plasma trace 12-hr back in time. The color of the circles represent the history of the vTEC along this trace. The plasma 12-hr prior to the event

FORSYTHE ET AL. 6 of 19

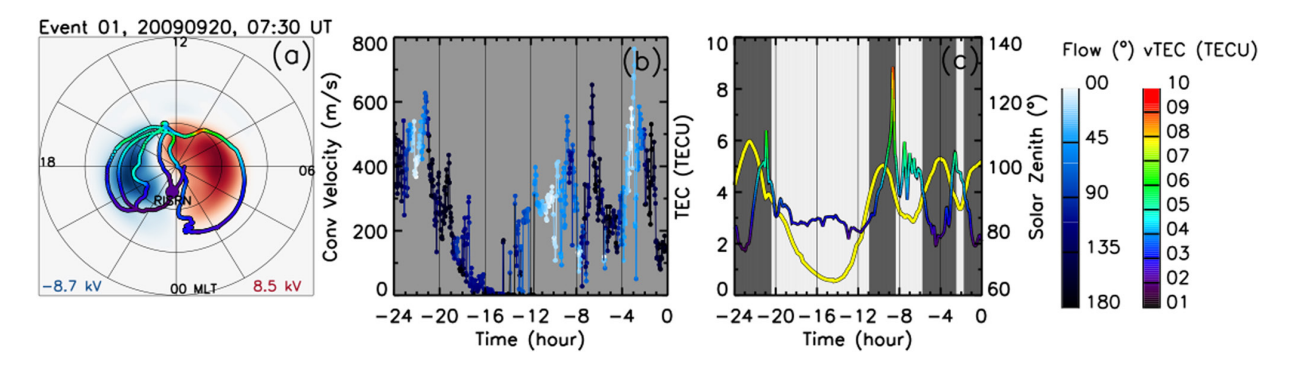


Figure 6. (a) The background color shows the SuperDARN potential map for the time that corresponds to the middle of the polar hole events, shown in Figure 3a. The minimum and maximum values of the potential are shown at the bottom. Large circle shows the location of the radar, and the test particle injection point. The trace shows the 24-hr history of the plasma motion, color coded in vTEC from the IDA4D with the color bar shown on the right of the figure. (b) The magnitude of the convection velocity along the trace, color coded in flow angle, with the color bar located on the right of the figure. The flow angle of 0° corresponds to the sun-ward direction. (c) The vTEC along the trace is shown with colored curve. Yellow curve shows the SZA at 300 km of altitude along the trace. The white, gray, and black color of the background indicates that the plasma is moving in the sunlit, twilight, and fully dark conditions.

arrived from the sunlit place with high vTEC (shown with dark red circles), it traveled along the left convection cell, and reached low plasma content during its anti-sunward way through the polar cap. The gray circle shows the RISR-C location 1 hr after, at 8:00 UT, with the 12-hr trace of plasma. In this case, the plasma completed two full circles around the right convection cell. It had lower electron content along the way in comparison to the other trace, however, the lowest electron content was also achieved at the final path through the polar cap, going in the anti-sunward direction.

Next, the vTEC, magnitude and direction of the convection velocity, and the SZA along the traces for all nine events are analyzed. Figure 6 shows the plasma trace for the first event. The test particle was injected in the middle of the depletion observed by RISR-N, which corresponded to 7:30 UT. The configuration of the convection at this time instance is shown with color in Figure 6a, whereas the lowest and the highest values of the potential is shown at the bottom of the panel. Figure 6a also shows the location of the radar (circle) and the 24-hr plasma trace color-coded in IDA4D vTEC, with the color bar shown on the right of the Figure. Figure 6b shows the magnitude of the plasma convection along the trace color coded in plasma flow direction. The black and white colors indicate the anti-sunward and sunward flows, respectively. Figure 6c also shows the vTEC along the trace as a function of time prior to the arrival of the depletion to the radar's field of view. A yellow curve in Figure 6c shows the SZA along the trace. The white, gray and black areas of the background indicate the periods of sunlight, twilight, and full darkness. Figures 7 and 8 shows the other 8 events in the same format as Figure 6.

As can be seen from Figures 6, 7, and 8, there is no preferable path of the plasma prior to the depletion. In some cases (Events 3, 4, and 6) the plasma circles around the left convection cell several times, in other case (Event 5) around the right cell, and in one case (Event 1) the mixture of both. For these events the magnitude of the convection velocity is fairly large, often exceeding 400 m/s, to travel these long ways. In several cases (Events 2, 8, and 9) the plasma moves slower and barely makes one closed loop in 24 hr, together with the one case (Event 7) of very slow plasma motion that moved without completing even one closed loop in 24-hr time frame.

Looking at the direction of the plasma velocity along the trace, shown in panel (b) of Figures 6, 7, and 8, it can be noticed that the flow is anti-sunward (black color) several hours prior to the arrival into the radar's field of view. However, since many events have closed loops, the sunward flow is present as well.

Looking at the vTEC and the SZA along the trace, shown in panel (c), the expected anti-correlation is present in most of the cases. Meaning that the vTEC increases when the plasma flows in the sunlit places, decreasing during the path through the shadow and the full darkness due to the lack of production. Events 2, 3, and 7, are good examples of the expected behavior. There are, however, some unexpected depletions that were observed even in the sunlit sectors. For example, 20 to 12 hr before the depletion detection in event number 1, where the slow-moving plasma depleted to 3 TECU in the sunlit environment. Oppositely, there are incidents of high vTEC together with the high SZA, for example, events number 5, 6, 8, and 9. This could be due to the presence of the polar patches

FORSYTHE ET AL. 7 of 19

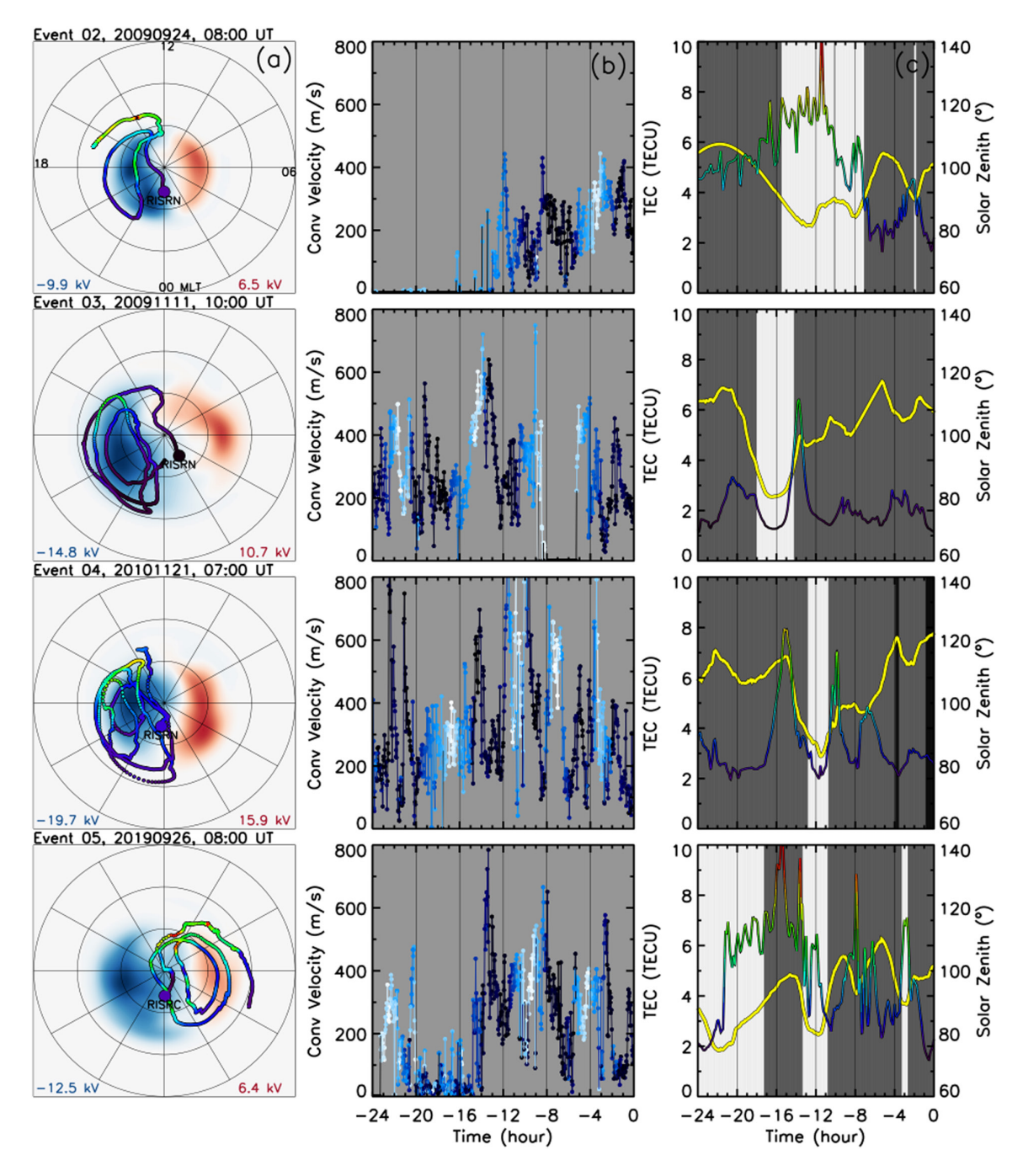


Figure 7. Events 2–5, same format as Figure 6.

or/and particle precipitation. Interestingly, the full darkness, when the SZA exceeds 120° is not abundant in the events, and the twilight conditions are often enough to deplete the plasma.

The analysis above has demonstrated that it requires approximately four hours to deplete the plasma that arrives from the day-side. To further investigate this point, multiple traces were found for the time when the ISR observed the depleted region. More specifically, the 4-hr long traces were found for all time frames between the white dashed lines in Figure 3. Figure 9 shows the traces for all 9 events. The background shows the sunlight, twilight

FORSYTHE ET AL. 8 of 19

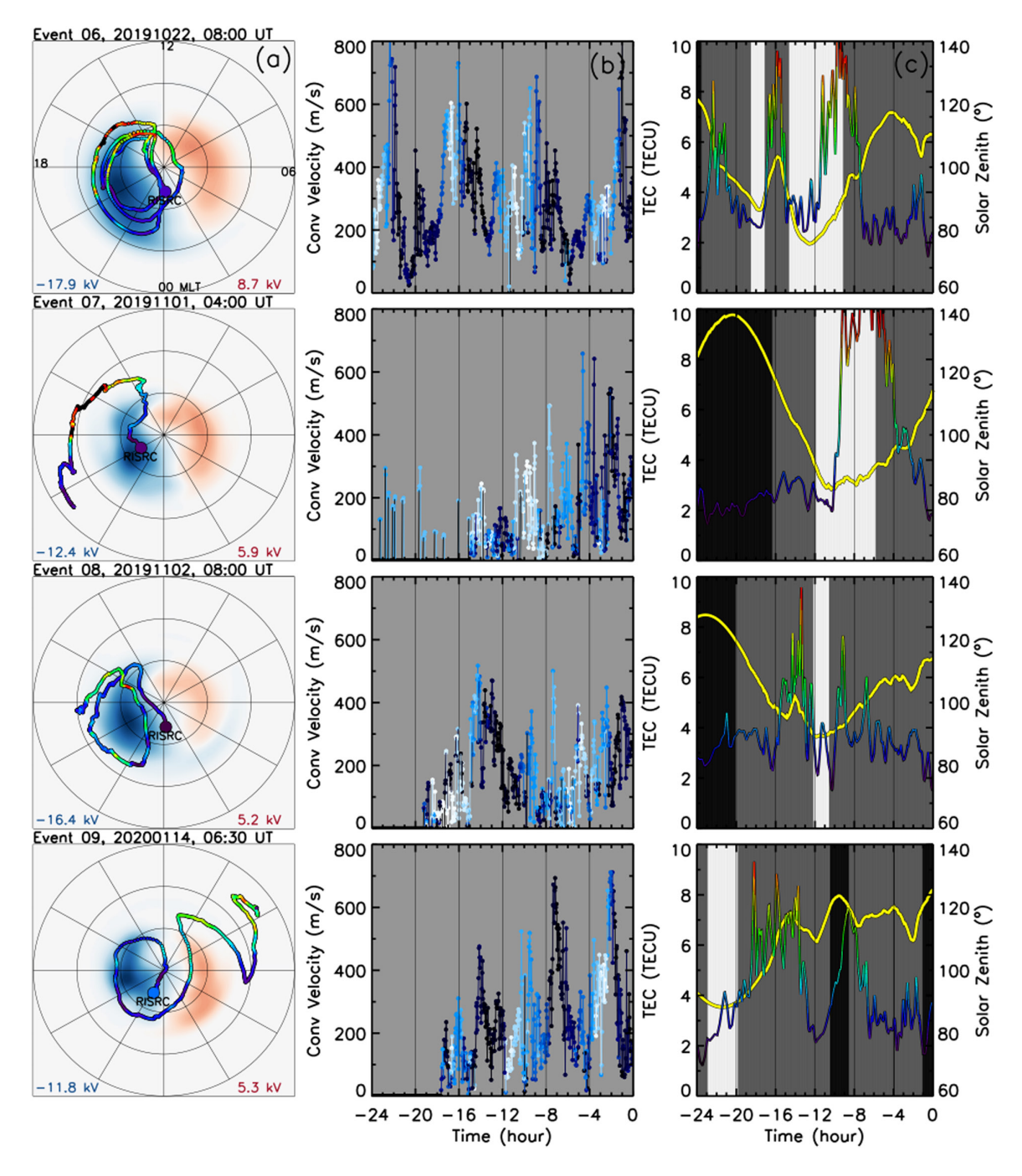


Figure 8. Events 8-12, same format as Figure 6.

and full darkness conditions for the beginning of the event. The large circles show the last point in trace that is the radar location that moves with time. The traces are color-coded in vTEC, as before. Figure 9 demonstrates that the full darkness was not necessary at least for 6 events. Only events number 3, 4, and 9 had the plasma traveled in the full darkness prior to the ISR observation.

FORSYTHE ET AL. 9 of 19



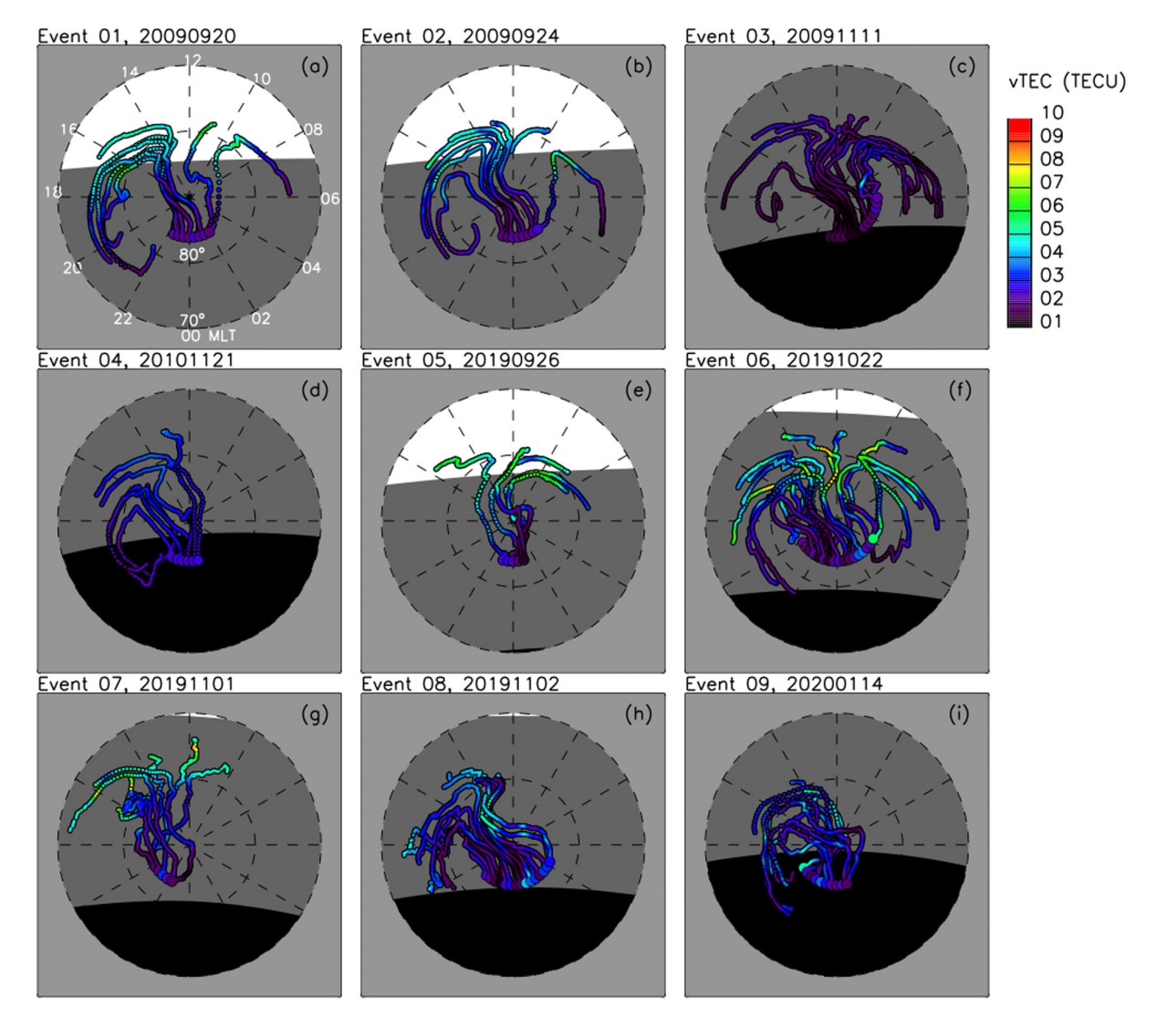


Figure 9. The 4-hr history of plasma motion prior to the radar's observation for the full length of the observed events. The background shows the sunlight, twilight, and full darkness by white, gray and black colors, respectively.

Figure 10 shows the forward motion of plasma after the radar's observation. In all the events the plasma continues moving toward the night sector and in the case of events 1, 2, and 3 makes its way back toward the dayside. Other events present the classical description of the polar hole (Brinton et al., 1978), where the plasma moves through the full darkness. Events number 1 and 8 show some presence of Harang discontinuity (Harang, 1946; Zou et al., 2009). However, the vTEC level at these traces doesn't show a particular change and stays at similar level as at the other traces.

3.1. Number of Convection Cells

To investigate the hypothesis that the configuration of the plasma convection with multiple convection cells increase the occurrence of density depletions, the following analysis was performed. The SuperDARN maps of electrostatic potential Φ were inverted to obtain $-|\Phi|$ and then the watershed operator was applied to the map to find the boundaries of the watersheds. Figure 11a and 11b show two snapshots of the electrostatic potential from event 7, November 1, 2019, at 00:42 UT and 13:27 UT, respectively. Black dots show the boundaries of the

FORSYTHE ET AL. 10 of 19



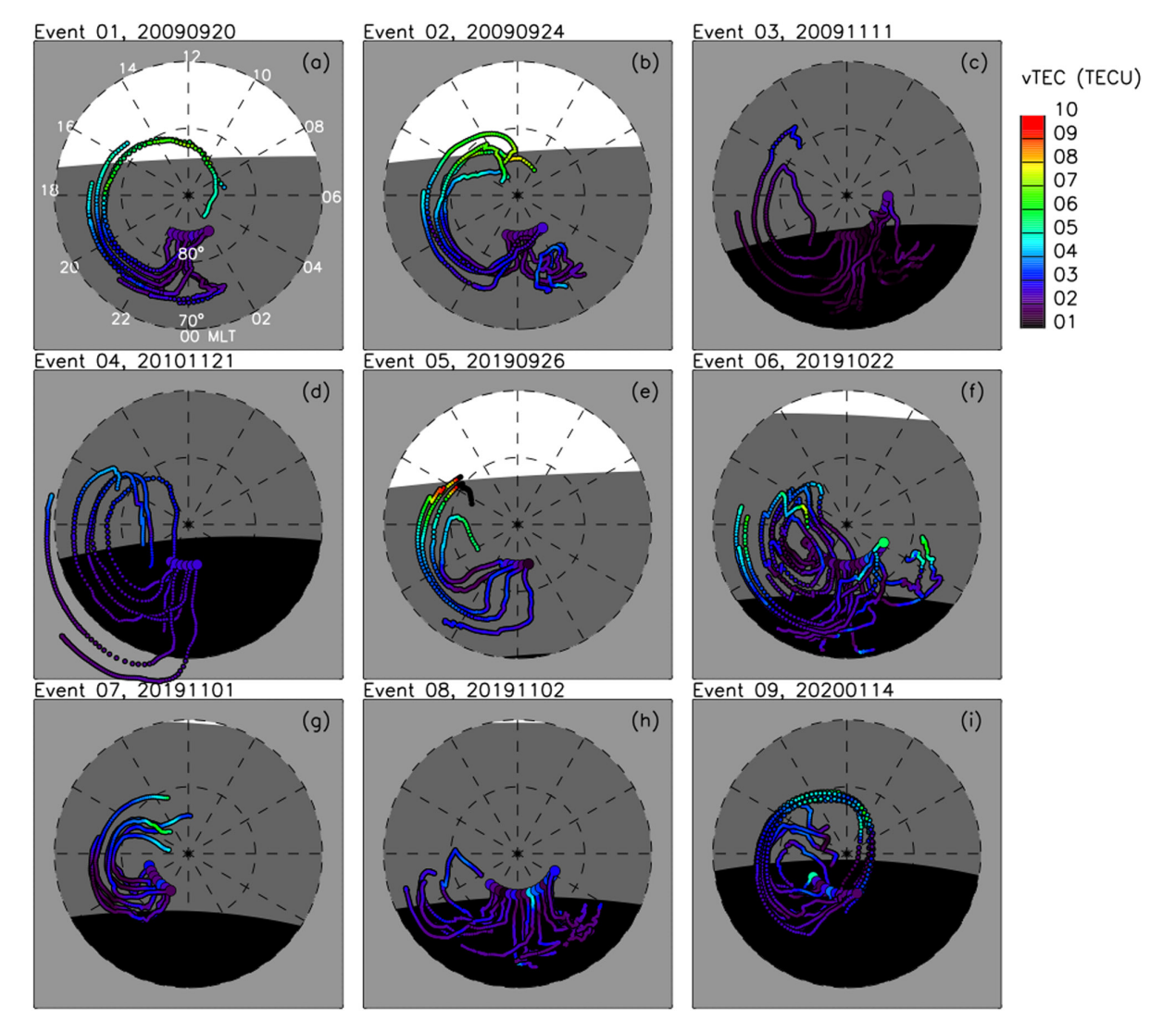


Figure 10. Same format as Figure 9 with the traces indicating the motion of plasma forward in time after being observed by the radar.

watersheds. The regions with main minimum and maximum are indicated with large black circles. Figures 11a represents an example of a standard two-cell convection configuration. In this simple case, the watershed operator identifies two cells. A more complicated example is shown in Figures 11b, where the watershed operator identifies 11 different regions. However, some of the regions represent the distortion of the two main cells, rather than separate cells. In order to exclude the distortions the following steps were performed. The differences between the local minima (maxima) and main minimum (maximum) for each region is calculated. The region considers a cell in case this difference exceeds a nominal value of 3 kV. For example, in Figures 11b the cell with local minima of -11.2 kV is not counted and grouped together with the main minimum cell of -12 kV. The additional cells that were counted are indicated by small black circles. As a result, the number of cells that were counted as separate cells was equal to 7 for the example shown in Figures 11b. This approach gives a robust estimation for the number of convection cells, that would indicate the deviation from the standard two-cell configuration, shown in Figures 11a.

Figure 12 shows the 30-min averaged number of the convection cells 24-hr prior to the detection of the polar hole. Events number 1, 2, 3, and 6 show a very minimal deviation of the convection from the two-cell configuration. Whereas, events 7, 8, and 9 show significant distortion of the cells half a day prior to the depletion formation.

FORSYTHE ET AL. 11 of 19



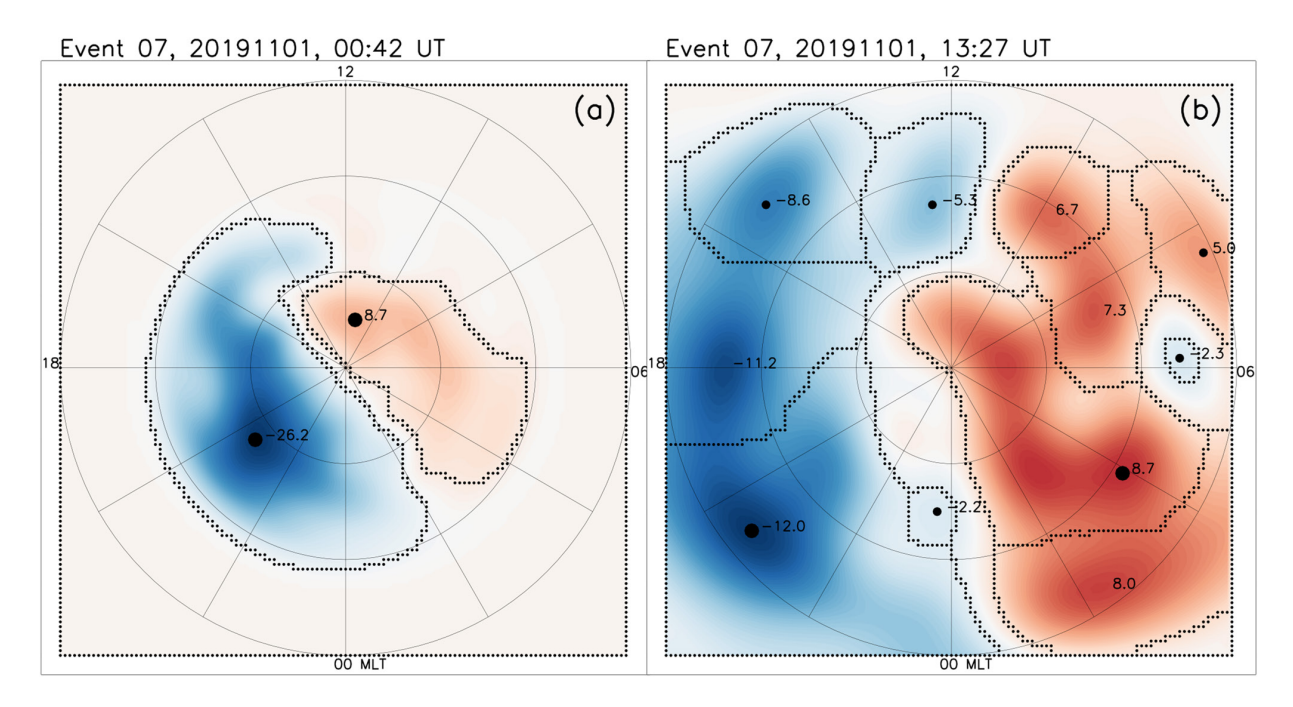


Figure 11. An example of the watershed operator applied to determine the number of the convection cells. The background shows the snapshot of the SuperDARN electrostatic potential for the event number 7, November 1, 2019 at (a) 00:42 UT and (b) 13:27 UT. The values of the potential at all local minima and maxima are shown in kV. Black dots show the boundaries of the watershed regions. The large black circles indicate the regions of minimum and maximum, and smaller black circles show the regions that are considered as additional convection cells.

However, the convection returns back to normal configuration about 6 hr prior to the polar hole detection. This analysis confirms that multiple cell configuration of the convection is not necessary for the formation of the polar holes.

3.2. MLT and Latitudinal Extent of the Depletion

Further, the MLT extent of the low density regions is investigated for all the events using the results of IDA4D. Figures 13a, 13b, and 13c show the vTEC at 80°N, 70°N, and 60°N magnetic latitude, respectively, for event 1. Black dots in Figure 13 show the beginning and the end of the region where the vTEC is less than 2 TECU, whereas the white dots show the middle position of this region. The gray line in Figure 13a shows the MLT position of RISR-N, projected to 80°N MLat, and the two dashed lines show the time period when the depletion was observed by the radar, same as in Figure 3a. The timing when the depletion is being observed by RISR-N agrees well with the position of low vTEC obtained by IDA4D run. Further in text, the region with vTEC less then 2 TECU is referred to as a polar hole region. It is evident from Figure 13a that the polar hole region was formed prior to the RISR-N detection, at 3 UT and existed for about 7 hr. The polar hole region was located between 21–06 MLT, similar to the statistical location of the polar hole (Brinton et al., 1978). Interestingly, the latitudinal extent of that region goes all the way down to 60°N, if not further, as can be seen from Figures 13b and 13c. At lower latitudes, the depleted region was present during most UTs slightly increasing its electron content between 13–18 UT at 70°N and between 12:30–14:30 UT at 60°N. The MLT extent of the depleted region was approximately the same at all three latitudes.

To analyze the latitudinal extent of the depletion, the vTEC along the fixed MLT of 1:30 is considered. Figure 14 shows the latitudinal variation of vTEC during the day of the event 1. Similar to Figure 13, the black lines with dots show the upper and lower boundary of the region where vTEC is less than 2 TECU, wheres the white line with dots show the middle of this region. A gray dot shows the location of RISR-N at 01:16 MLT, and white dashed lines show the beginning and the end of the depletion as observed by the radar. Figure 14 shows that the polar hole is not a separate region of low density that appears in the polar cap. It rather represents a

FORSYTHE ET AL. 12 of 19

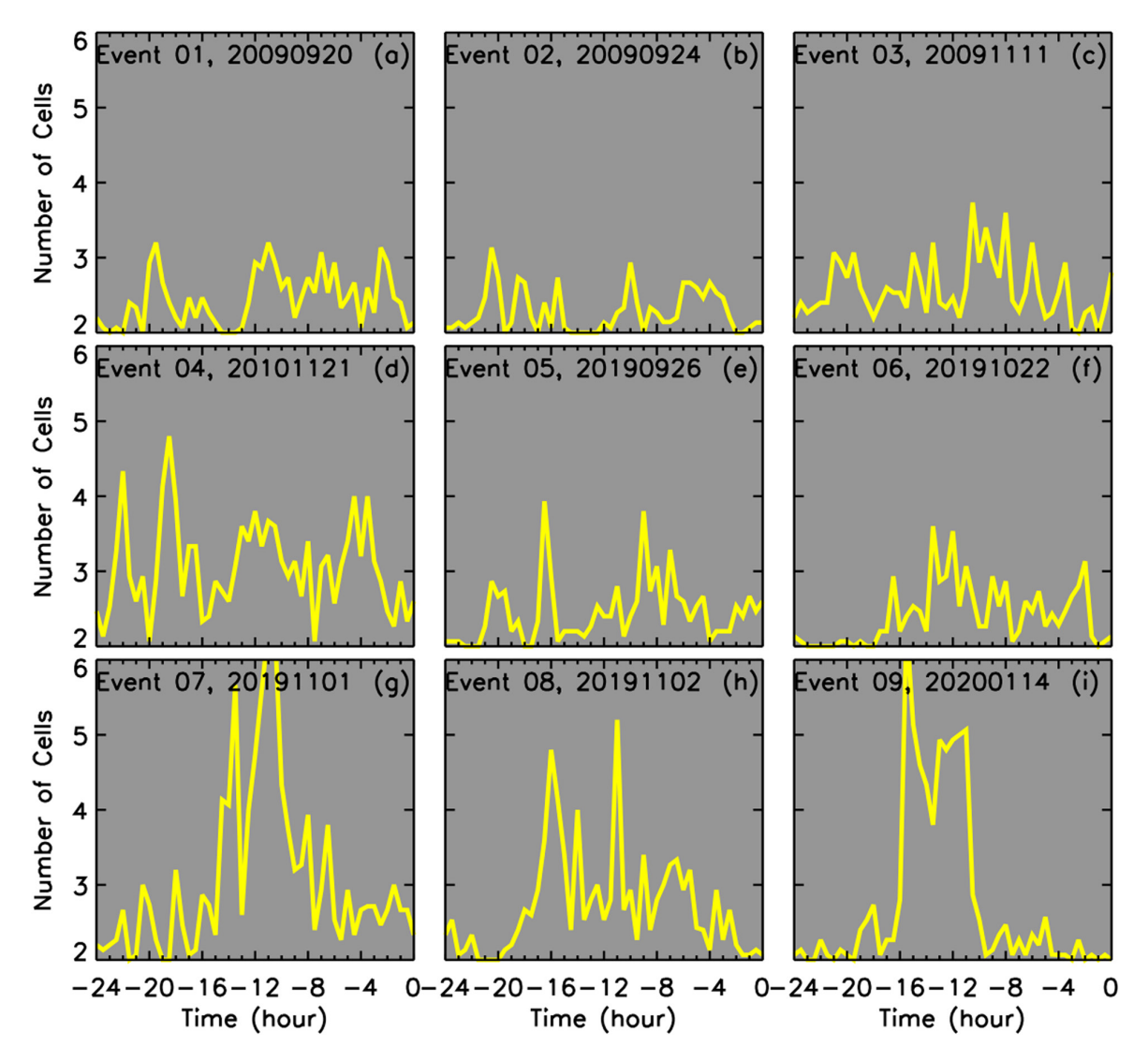


Figure 12. The number of the convection cells prior to the event detection averaged every 30 min.

stable presence of the depleted density at 60° – 70° N that becomes extended and shifted to the higher latitudes $(70^{\circ}$ – 90° N) from 2–10 UT.

Figure 15 shows the MLT and latitudinal extent of the depletion averaged between the events. Figure 15a shows the sketch of the depletion, defined by the region with vTEC less than 2 TECU. Figures 15b, 15c, and 15d show the averaged MLT extent of the depleted region, along 80°, 70°, and 60°N, respectively. The colored curves indicate the boundaries of the region, shown with colored circles in Figure 15a, whereas the black curves show the center of the region. Figure 15e shows the latitudinal extent of the depleted region along the fixed at 01:30 MLT, which is an averaged among all events MLT location of the polar hole center at 80° and 70°N. The averaged among all events parameters characterizing the MLT and MLat extent of the depleted region show similar trend with the event number 1, discussed above. The MLat location of the density depletion is relatively stable during the day at 70° and 60°N, ranging between 0–4 MLT, with its boundaries spreading between 21 and 6 MLT (Figures 15c and 15d), same as for the statistical location of the polar hole (Brinton et al., 1978). The center of the depletion region extends poleward to 70°–80°N between 2–9 UT, Figure 15e. Around that portion of the day, the MLT extent of the depletion can be determined at 80°N, Figure 15b. The center of the depletion shifts closer to 0

FORSYTHE ET AL. 13 of 19

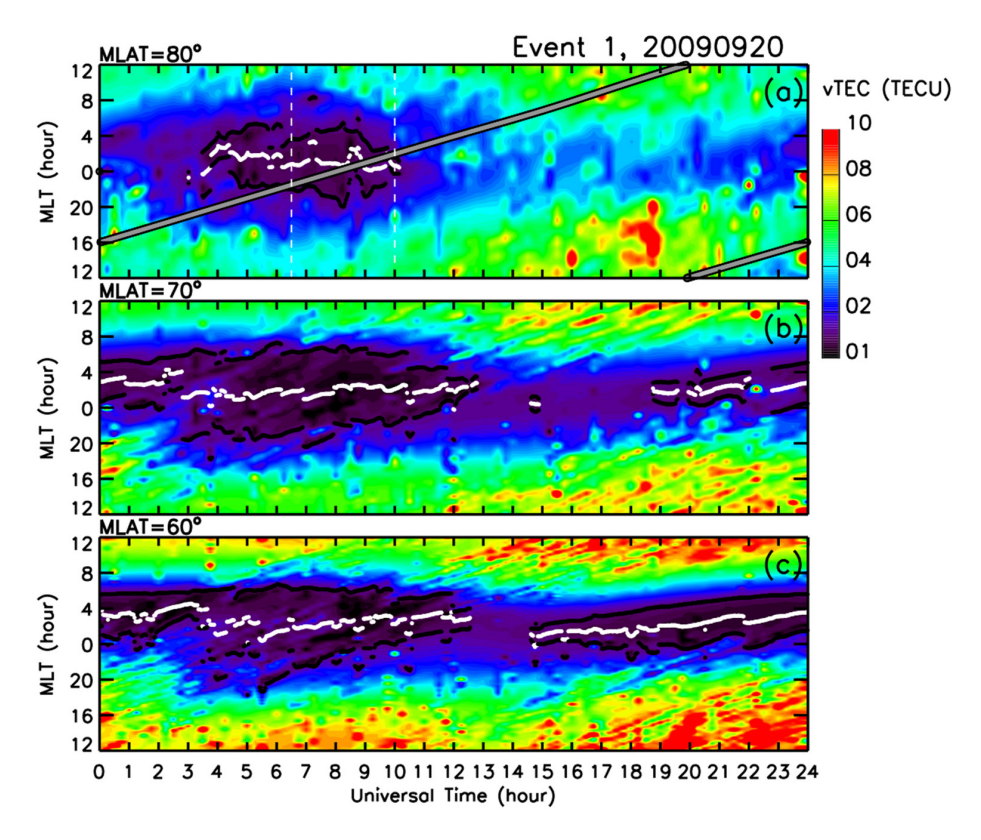


Figure 13. The MLT extent of the density depletion along (a) 80° , (b) 70° , and (c) 60° of magnetic latitude. The color shows the vTEC from IDA4D with the color bar shown on the left of the figure. Black dots show the beginning and the end of the region with vTEC less then 2 TECU, whereas the white dots show the center of this region. The gray line in panel (a) shows the MLT location to RISR-N. Two dashed lines in panel (a) show the period when RISR-N observed the depletion, same as in Figure 3a.

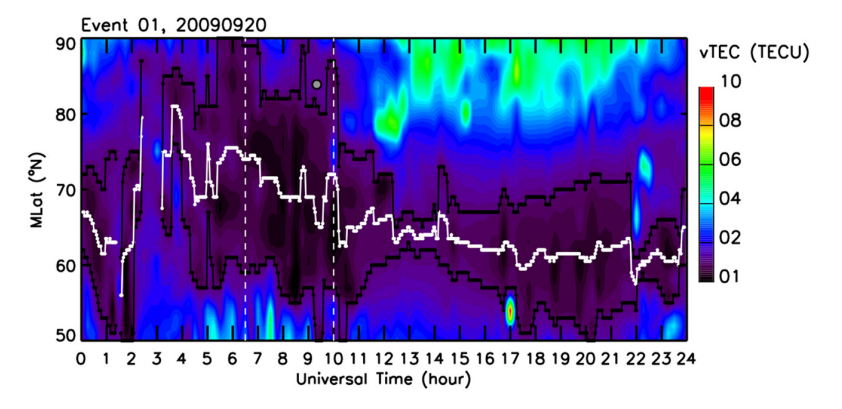


Figure 14. The Latitudinal extent of the density depletion at fixed MLT, that is an average location of the depletion at 80°N MLat. For the event number 1 it is 01:16 MLT. The color shows the vTEC from IDA4D with the color bar shown on the left of the figure. Black dots show the beginning and the end of the region with vTEC less then 2 TECU, whereas the white dots show the center of this region. The gray line shows the MLat location of RISR-N. Two dashed lines show the period when RISR-N observed the depletion, same as in Figure 3a.

FORSYTHE ET AL. 14 of 19



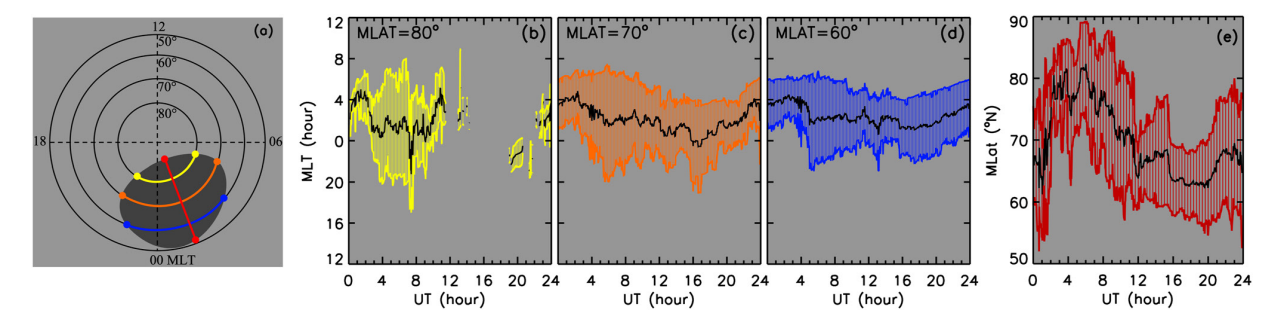


Figure 15. (a) Sketch that shows a density depletion, defined by the region with vTEC less than 2 TECU. The MLT extent of the depletion is determined along 80°, 70°, and 60°N, which is shown with yellow, orange, and blue curves, respectively. The latitudinal extent of the depletion is measured through the fixed 01:30 MLT, which is an averaged center of the yellow and orange curves. Panels (b–d) show the MLT boundaries of the depleted region, indicated with circles in panel (a), for MLat of 80°, 70°, and 60°N, respectively. Panel (e) shows the latitudinal extent of the depletion. The black curves in panels (b–e) show the center of the depletion.

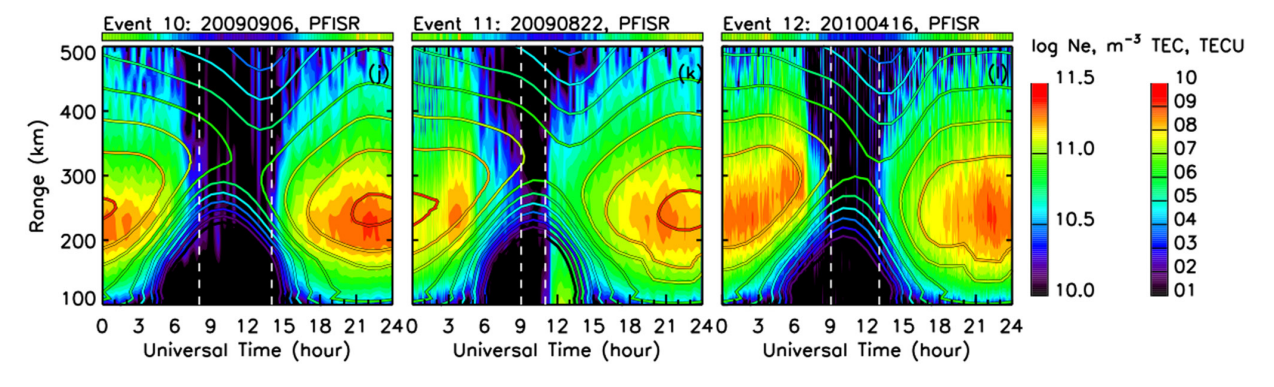
MLT around that time of the day, with similar MLT extent as at the lower MLats. Most importantly, the averaged values between all 9 events show that the depletion does not appear in the expected location of the statistical polar hole independently, but rather presents the latitudinal shift or extension of the depletion from sub auroral sector to the polar cap region.

3.3. Low Density Events Observed by PFISR

Using similar criteria, three low-density events were found using PFISR data. Figure 16 shows the observed depleted regions in the same format as in Figure 3. The events look very similar to the cases observed by RISR-N and RISR-C radars. The F-region layer almost fully disappears for more than two hours. The analysis of the convection measurements are shown in Figure 17, that has the same format as Figure 6. The plasma becomes depleted on its way from the polar cap to the radar's location, slowly traveling anti-sunward in the twilight zone. The slow convection flow prior to the detection of the depletion is more pronounced in these events in comparison to the events detected by RISR. Figure 18 demonstrates the averaged among three events extent of the depletion in the same format as Figure 15. The MLT position of the depletion looks similar to the RISR events. The MLat variation of the depletion's location during the day of the events has similar trend as in Figure 15e, with the poleward shift around 4 UT, however, the overall latitudinal position of the depletion, including the shift to the higher latitudes, is about 5° –10° lower than was observed for the RISR events.

4. Discussion

This study experimentally demonstrated that the density depletions observed in the polar cap region have large latitudinal extent and are directly connected to the low density regions located between MLat of 60–70°N. Another density depletion events, known as high-latitude troughs, can occur in this latitudinal region. The ionospheric



 $\textbf{Figure 16.} \ \ \text{Events found with PFISR data; same format as Figure 3}.$

FORSYTHE ET AL. 15 of 19



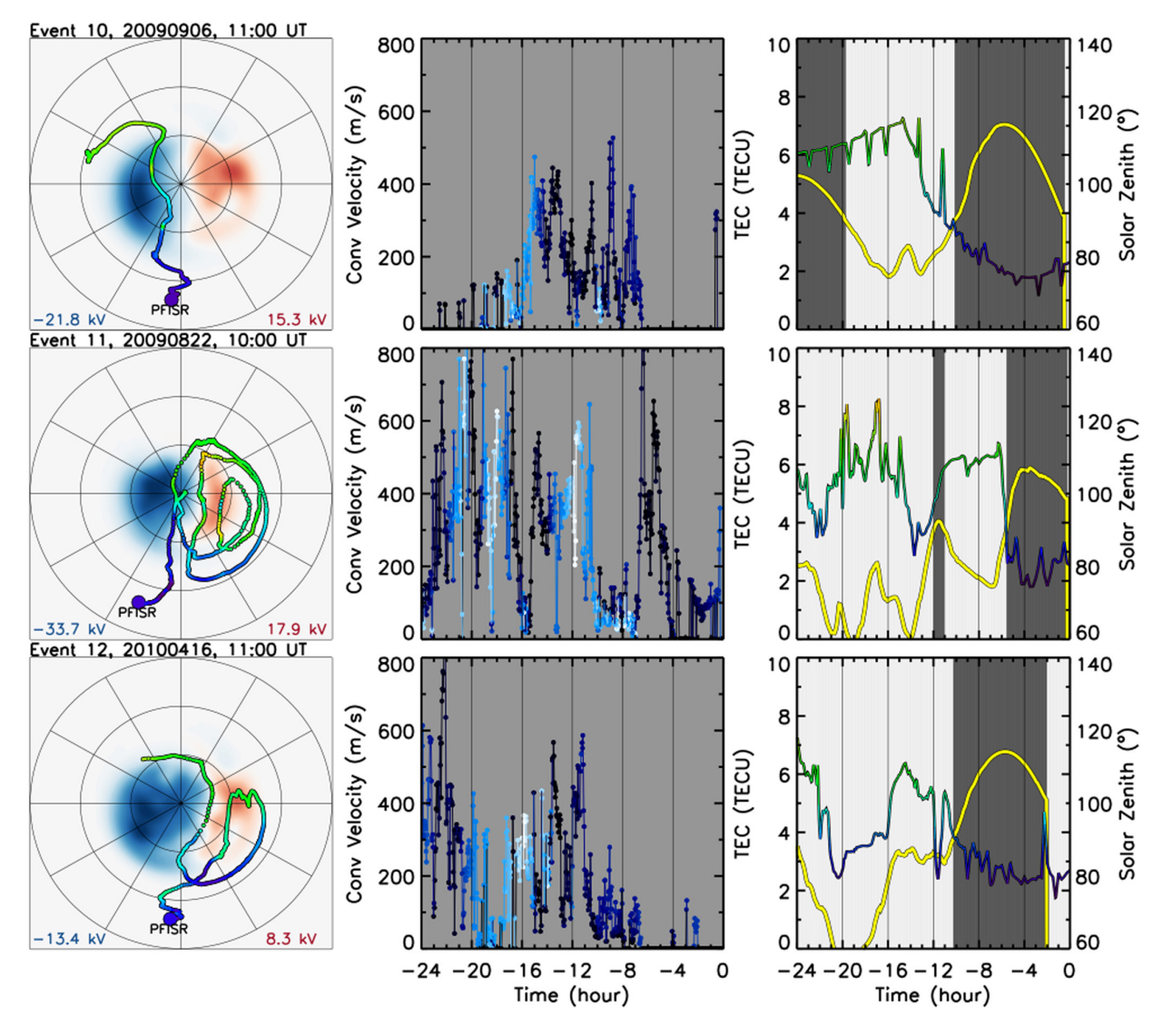
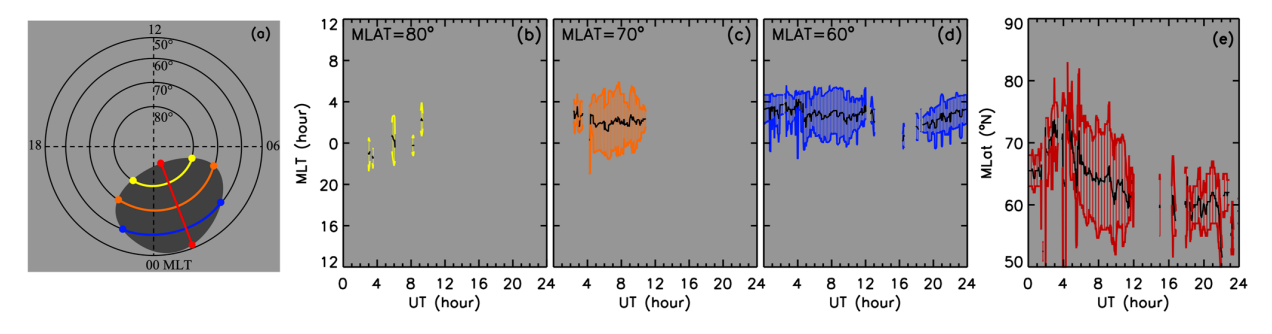


Figure 17. Same as Figure 6 for events found with PFISR data.



 $\textbf{Figure 18.} \ \ \text{Same format as Figure 15 for events found with PFISR data}.$

FORSYTHE ET AL. 16 of 19

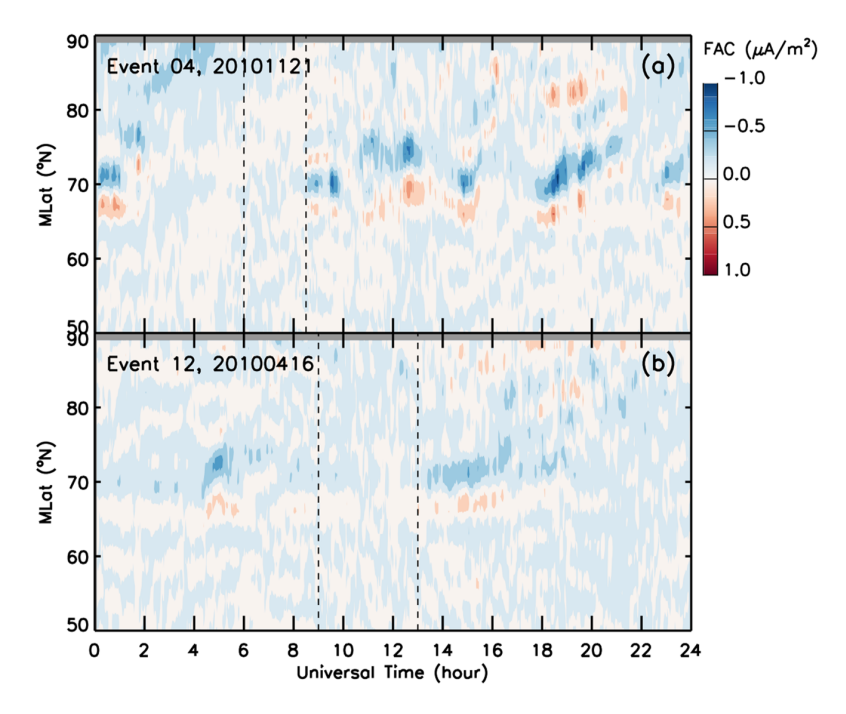


Figure 19. The FACs along the fixed MLT of 2 hr as a function of magnetic latitude and UT. The dashed lines indicate the beginning and the end of the polar hole observed by ISR.

troughs are regions of exceptionally low electron density at subauroral and auroral latitudes. Whereas the high-latitude troughs are defined as density depletions located withing the auroral oval or the polar cap (Jones et al., 1990; Rodger et al., 1992), while the mid-latitude troughs are located equatorward of the auroral oval. The high-latitude troughs are usually accompanied by enhanced eastward convection flows (Zou et al., 2016), significantly enhanced ion temperature, no change or a decrease in the electron temperature, large upward field-aligned ion velocity (Ma et al., 2000; Williams & Jain, 1986; Winser et al., 1986) and downward field aligned currents (FACs) (Zou et al., 2016).

In order to check the connection of the polar holes observed in this study to the high-latitude troughs, the FACs derived from Active Magnetosphere and Planetary Electrodynamics Response Experiment (AMPERE) (Anderson et al., 2014) observing system were employed. The AMPERE outputs were available for two events: event number 4 observed by RISR, and event 12 observed by PFISR. Figure 19 shows the FACs along fixed MLT of 2 hr as a function of magnetic latitude and UT. For both events, the FACs were very weak at the time periods when the polar holes were observed by RISR and PFISR, shown with black dashed lines in Figure 19. Additional check of the plasma temperature data from RISR showed that for all events the plasma temperature was slightly lower than the temperature of the surrounding regions, indicating the lack of precipitation and frictional heating inside the polar holes. Finally, the Special Sensor Ultraviolet Spectrographic Imager (SSUSI) online tool was used to check whether the equatorward boundary of the auroral oval is located lower than the lowest latitudinal boundary of the polar holes. All nine events detected by RISR system were located poleward of the auroral oval, while the three events detected by PFISR were located equatorward of the auroral oval. Therefore, the absence of strong downward FACs, precipitation, and frictional heating indicates that all the events observed by RISR in this study belong to the category of classical polar holes formed mainly due to the lack of production. The events observed by PFISR belong to the category of the subauroral depletions formed due to the lack of production.

Due to the location of the RISR and PFISR, the found events represented the two extremes of the density depletion locations. Perhaps, if an additional ISR radar was located in latitudinal region between the two existing radars (at 75°N) significantly more polar hole events could be detected, including the one produced in the region of Harang plasma flow reversal, seen in Figure 10.

FORSYTHE ET AL. 17 of 19



This paper draw similar conclusion to the results of Makarevich et al., (2015), that neither slow or fast convection flows are associated with the polar depletions. Among 12 events presented in this paper, six polar holes were adjacent to the enhanced convection 4-hr prior to the detection, as was shown in Figures 6, 7 and 8.

5. Conclusion

In this study nine polar holes were found in the polar cap region and three depletions were detected in sub auroral region. Implementing the multi-instrument analysis using ISR data, SuperDARN data, and data assimilation IDA4D algorithm, the following conclusions were derived:

- 1. Plasma does not have to be trapped in the closed convection cells to be depleted
- 2. Full darkness is not necessary, and a polar hole can be produced in the twilight zone
- Half of the time the polar holes were adjacent to the enhanced convection associated with higher plasma density
- 4. Standard two-cell convection configuration was present during polar hole events, with an exception of three events when the convection pattern was distorted 8-hr prior to the extension of the depleted region to the polar cap region
- 5. The investigated depletions were located between 6 and 21 MLT, in agreement with the statistical polar hole location
- 6. The polar holes observed with RISR were on average located between 65° and 90° N part of the day, further shifting down to lower latitudes of 60° – 70° N
- 7. The density depletions observed with PFISR exhibited similar behavior, but initially stayed below 80°N

Further studies will be conducted to investigate the internal structuring of the depleted regions and their effects on the HF signal propagation in the polar cap and auroral regions.

Data Availability Statement

The SSUSI outputs are available at http://cedar.openmadrigal.org/openmadrigal. The Iridium-derived AMPERE data used in this paper can be obtained from the AMPERE Science Center at http://ampere.jhuapl.edu/. The GPS RINEX data were obtained through the online archives of the Crustal Dynamics Data Information System (CD-DIS), NASA Goddard Space Flight Center, Greenbelt, MD, USA. http://cddis.gsfc.nasa.gov/. The vTEC outputs of IDA4D analyzed in this study can be found at https://doi.org/10.5281/zenodo.5338621. The post processed convection maps used in this study can be found at https://doi.org/10.5281/zenodo.5338814.

Acknowledgments

This work was supported by NSF grant AGS-2022159. S. Zou acknowledges NASA Grant 80NSSC20K1313. RISR and PFISR data was obtained through Madrigal Database http://ccdar.openmadrigal.org/openmadrigal. The authors acknowledge the use of SuperDARN data. SuperDARN is a collection of radars funded by national scientific funding agencies of Australia, Canada, China, France, Italy, Japan, Norway, South Africa, United Kingdom and the United States of America. The SuperDARN convection maps are available at http://vt.superdarn.org.

References

Anderson, B. J., Korth, H., Waters, C. L., Green, D. L., Merkin, V. G., Barnes, R. J., & Dyrud, L. P. (2014). Development of large-scale birkeland currents determined from the active magnetosphere and planetary electrodynamics response experiment. Geophysical Research Letters, 41, 3017–3025. https://doi.org/10.1002/2014GL059941

Bahcivan, H., Tsunoda, R., Nicolls, M., & Heinselman, C. (2010). Initial ionospheric observations made by the new resolute incoherent scatter radar and comparison to solar wind IMF. *Geophysical Research Letters*, 37, L15103. https://doi.org/10.1029/2010GL043632

Benson, R. F., & Grebowsky, J. M. (2001). Extremely low ionospheric peak altitudes in the polar hole region. Radio Science, 36, 277–285. https://doi.org/10.1029/1999rs002401

Bilitza, D., Altadill, D., Truhlik, V., Shubin, V., Galkin, I., Reinisch, B., & Huang, X. (2017). International Reference Ionosphere 2016: From ionospheric climate to real-time weather predictions. *Space Weather*, 15, 418–429. https://doi.org/10.1002/2016sw001593

Brinton, H. C., Grebowsky, J. M., & Brace, L. H. (1978). The high-latitude winter F region at 300 km - Thermal plasma observations from AE-C. Geophysical Research Letters, 83, 4767–4776. https://doi.org/10.1029/JA083iA10p04767

Bust, G. S., Coco, D., & Makela, J. J. (2000). Combined Ionospheric Campaign 1: Ionospheric tomography and GPS total electron count (TEC) depletions. *Geophysical Research Letters*, 27(18), 2849–2852. https://doi.org/10.1029/2000GL000053

Bust, G. S., Coco, D. S., & Gaussiran, T. L., II. (2001). Computerized ionospheric tomography analysis of the Combined Ionospheric Campaign. Radio Science, 36(6), 1599–1605. https://doi.org/10.1029/1999RS002424

Radio Science, 36(6), 1599–1605. https://doi.org/10.1029/1599RS002424

Bust, G. S., & Crowley, G. (2007). Tracking of polar cap ionospheric patches using data assimilation. Journal of Geophysical Research, 112, 1–17. https://doi.org/10.1029/2005JA011597

Bust, G. S., & Datta-Barua, S. (2014). Scientific Investigations Using IDA4D and EMPIRE. chap. 23 (pp. 283–297). American Geophysical Union (AGI). https://doi.org/10.1002/9781118704417.ch23

Bust, G. S., Garner, T. W., & Gaussiran, T. L. (2004). Ionospheric Data Assimilation Three-Dimensional (IDA3D): A global, multisensor, electron density specification algorithm. *Journal of Geophysical Research*, 109, 1–14. https://doi.org/10.1029/2003JA010234

Bust, G. S., & Mitchell, C. N. (2008). The history, current state, and future directions of ionospheric imaging. *Reviews of Geophysics*, 46, 1–23. https://doi.org/10.1029/2006RG000212

FORSYTHE ET AL. 18 of 19



- Carlson, H. C. (2012). Sharpening our thinking about polar cap ionospheric patch morphology, research, and mitigation techniques. Radio Science, 47, 1–16. https://doi.org/10.1029/2011RS004946
- Chisham, G., Lester, M., Milan, S. E., Freeman, M. P., Bristow, W. A., Grocott, A., et al. (2007). A decade of the Super Dual Auroral Radar Network (SuperDARN): Scientific achievements, new techniques and future directions. Surveys in Geophysics, 28, 33–109. https://doi.org/10.1007/s10712-007-9017-8
- Crowley, G., Carlson, H. C., Basu, S., Denig, W. F., Buchau, J., & Reinisch, B. W. (1993). The dynamic ionospheric polar hole. *Radio Science*, 28, 401–413. https://doi.org/10.1029/92rs02878
- Daley, R., & Barker, E. (2000). The NAVDIS source book 2000: NRL atmospheric variational data assimilation system: Naval Research Laboratory
- Datta-Barua, S., Bust, G. S., & Crowley, G. (2011). Deducing storm-time F-region ionospheric dynamics from 3-D time-varying imaging. *Journal of Geophysical Research*, 116, 1–14. https://doi.org/10.1029/2010JA016304
- Evans, J. V. (1969). Theory and practice of ionosphere study by Thomson Scatter Radar. Proceedings of the IEEE, 57, 496–530. https://doi.org/10.1109/PROC.1969.7005
- Foster, J. C., Zou, S., Heelis, R. A., & Erickson, P. J. (2021). Ionospheric storm-enhanced density Plumes. chap. 6 (pp. 115–126). American Geophysical Union (AGU). https://doi.org/10.1002/9781119815617.ch6
- Greenwald, R. A., Baker, K. B., Dudeney, J. R., Pinnock, M., Jones, T. B., Thomas, E. C., et al. (1995). DARN/SuperDARN: A global view of the dynamics of high-latitude convection. Space Science Reviews, 71, 763–796. https://doi.org/10.1007/bf00751350
- Harang, L. (1946). The mean field of disturbance of polar geomagnetic storms. *Terrestrial Magnetism and Atmospheric Electricity*, 51(3), 353–380. https://doi.org/10.1029/TE051i003p00353
- Hoegy, W. R., & Grebowsky, J. M. (1991). Dependence of polar hole density on magnetic and solar conditions. Geophysical Research Letters, 96, 5737–5755. https://doi.org/10.1029/90JA02755
- Jones, G. O. L., Williams, P. J. S., Winser, K. J., & Lockwood, M. (1990). Chracteristics of the high-latitude trough. Advances in Space Research, 10, 191–196. https://doi.org/10.1016/0273-1177(90)90253-v
- Kinrade, J., Mitchell, C. N., Yin, P., Smith, N., Jarvis, M. J., Maxfield, D. J., et al. (2012). Ionospheric scintillation over Antarctica during the storm of 5?6 April 2010. Journal of Geophysical Research, 117. https://doi.org/10.1029/2011JA017073
- Koustov, A. V., Ullrich, S., Ponomarenko, P. V., Nishitani, N., Marcucci, F. M., & Bristow, W. A. (2019). Occurrence of F region echoes for the polar cap SuperDARN radars. Earth Planets and Space, 71, 1–17. https://doi.org/10.1186/s40623-019-1092-9
- Ma, S. Y., Liu, P., & Schlegel, K. (2000). EISCAT observation of a highlatitude ionization trough associated with a reversed westward plasma flow. Geophysical Research Letters, 27, 3269–3272. https://doi.org/10.1029/2000g1000073
- Makarevich, R. A., Lamarche, L. J., & Nicolls, M. J. (2015). Resolute Bay Incoherent Scatter Radar observations of plasma structures in the vicinity of polar holes. *Journal of Geophysical Research*, 120, 7970–7986. https://doi.org/10.1002/2015JA021443
- Nicolls, M. J., Heinselman, C. J., Hope, E. A., Ranjan, S., Kelley, M. C., & Kelly, J. D. (2007). Imaging of polar mesosphere summer echoes with the 450 MHz Poker Flat Advanced Modular Incoherent Scatter Radar. Geophysical Research Letters, 34, 1–6. https://doi.org/10.1029/2007GL031476
- Oksavik, K., Barth, V. L., Moen, J., & Lester, M. (2010). On the entry and transit of high-density plasma across the polar cap. *Journal of Geophysical Research*, 115. https://doi.org/10.1029/2010JA015817
- Ren, J., Zou, S., Kendall, E., Coster, A., Sterne, K., & Ruohoniemi, M. (2020). Direct observations of a polar cap patch formation associated with dayside reconnection driven fast flow. *Journal of Geophysical Research: Space Physics*, 125, 1–16. https://doi.org/10.1029/2019JA027745
- Rishbeth, H., & Williams, P. J. S. (1985). The EISCAT ionospheric radar: The system and its early results. Quarterly Journal of the Royal Astronomical Society, 26, 478–512.
- Rodger, A. S., Moffett, R. J., & Quegan, S. (1992). The role of ion drift in the formation of ionisation troughs in the mid- and high-latitude ionosphere A review. *Journal of Atmospheric and Solar-Terrestrial Physics*, 54, 1–30. https://doi.org/10.1016/0021-9169(92)90082-v
- Ruohoniemi, J. M., & Baker, K. B. (1998). Large-scale imaging of high-latitude convection with Super Dual Auroral Radar Network HF radar observations, Journal of Geophysical Research, 103, 20797–20811. https://doi.org/10.1029/98ja01288
- Shepherd, S. G. (2014). Altitude-adjusted corrected geomagnetic coordinates: Definition and functional approximations. *Journal of Geophysical Research*, 119, 7501–7521. https://doi.org/10.1002/2014JA020264
- Sojka, J. J., Raitt, W. J., & Schunk, R. W. (1981b). Theoretical predictions for ion composition in the high-latitude winter F-region for solar minimum and low magnetic activity. *Journal of Geophysical Research*, 86, 2206–2216. https://doi.org/10.1029/ja086ia04p02206
- Sojka, J. J., Raitt, W. J., & Schunk, R. W. (1981c). Plasma density features associated with strong convection in the winter high-latitude F region. Journal of Geophysical Research, 86, 6908–6916. https://doi.org/10.1029/ja086ia08p06908
- Sojka, J. J., Raitt, W. J., & Schunk, R. W. (1981a). A theoretical study of the high-latitude winter F region at solar minimum for low magnetic activity. *Journal of Geophysical Research*, 86, 609–621. https://doi.org/10.1029/ja086ia02p00609
- Sojka, J. J., & Schunk, R. W. (1987). Theoretical study of the high? latitude ionosphere's response to multicell convection patterns. *Journal of Geophysical Research*, 92, 8733–8744. https://doi.org/10.1029/JA092iA08p08733
- Themens, D. R., Jayachandran, P. T., Nicolls, M. J., & MacDougall, J. W. (2014). A top to bottom evaluation of IRI 2007 within the polar cap. Journal of Geophysical Research: Space Physics, 119, 6689–6703. https://doi.org/10.1002/2014JA020052
- Thomas, E. G., Hosokawa, K., Sakai, J., Baker, J. B. H., Ruohoniemi, J. M., Taguchi, S., et al. (2015). Multi-instrument, high-resolution imaging of polar cap patch transportation. *Radio Science*, 50(9), 904–915. https://doi.org/10.1002/2015RS005672
- Williams, P. J. S., & Jain, A. R. (1986). Observations of the high latitude trough using EISCAT. Journal of Atmospheric and Solar-Terrestrial Physics, 48, 423–434. https://doi.org/10.1016/0021-9169(86)90119-4
- Winser, K. J., Jones, G. O. L., & Williams, P. J. S. (1986). A quantitative study of the high latitude ionospheric trough using EISCAT's common programmes. *Journal of Atmospheric and Solar-Terrestrial Physics*, 48, 893–904. https://doi.org/10.1016/0021-9169(86)90064-4
- Zou, S., Lyons, L. R., Wang, C.-P., Boudouridis, A., Ruohoniemi, J. M., Anderson, P. C., et al. (2009). On the coupling between the Harang reversal evolution and substorm dynamics: A synthesis of SuperDARN, DMSP, and IMAGE observations. *Journal of Geophysical Research*, 114, A01205. https://doi.org/10.1029/2008JA013449
- Zou, S., Moldwin, M., Nicolls, M., Ridley, A., Coster, A., Yizengaw, E., et al. (2016). Electrodynamics of the high-latitude trough: Its relationship with convection flows and field-aligned currents. *Journal of Geophysical Research: Space Physics*, 118, 2565–2572. https://doi.org/10.1002/jgra.50120

FORSYTHE ET AL. 19 of 19